Research Square

Preprints are preliminary reports that have not undergone peer review.
They should not be considered conclusive, used to inform clinical practice,
or referenced by the media as validated information.

Inverting Boundary Tractions on the Overriding Plate to Decouple Postseismic Deformation of the 2011 Mw 9.0 Tohoku-Oki Earthquake

Xianbing Zhang
Peking University
Yan Hu
University of Science and Technology of China https://orcid.org/0000-0002-5704-4827
Yongen Cai
yongen@pku.edu.cn

Peking University

Article

Keywords:

Posted Date: November 25th, 2026

DOI: https://doi.org/10.21203/rs.3.rs-11820242/v1

License: This work is licensed under a Creative Commons Attribution 4.0 International License.
Read Full License

Additional Declarations: There is **NO** Competing Interest. I declare that the authors have no competing interests as defined by Nature Portfolio

Inverting Boundary Tractions on the Overriding Plate to Decouple Postseismic Deformation of the 2011 Mw 9.0 Tohoku-Oki Earthquake

Xianbing Zhang[1], Yan Hu[2,3], Yongen Cai[1*]

1. School of Earth and Space Sciences, Peking University, Beijing 100871, China
2. Deep Space Exploration Laboratory, Hefei, Anhui 230088, China
3. National Key Laboratory of Deep Space Exploration, Hefei 230000, China

***Corresponding author: Yongen Cai (yongen@pku.edu.cn)**

Abstract

Quantifying how stress transfers among the fault, the overriding plate, and the mantle wedge following great megathrust earthquakes remains a fundamental challenge in subduction zone mechanics. Existing postseismic deformation and stress inversions typically treat the subduction system as a whole or rely on rheological assumptions. In contrast to previous studies, we develop a stress inversion method employing an elastic model restricted to the overriding plate. Using two years of GNSS/GNSS-A observations following the 2011 Mw 9.0 Tohoku-Oki earthquake, we invert for the tractions (stress changes) of the afterslip source, the locked source, and the mantle-wedge source (tractions exerted on the base of the model). The inversion results show that, in the second postseismic year of the earthquake relative to the first, the maximum shear stress decreased by 80% in the fault-afterslip zone and increased by 69% in the fault-locking zone. The areas of significantly reduced stress on the fault coincide with repeating-earthquake clusters, whereas the areas of markedly elevated stress correspond to the seismogenic zone and coseismic rupture area of the earthquake. Among the

surface displacements calculated from the inverted tractions, those caused by the locked, mantle-wedge, and afterslip sources are the largest (landward), intermediate (seaward), and smallest (seaward), respectively.

Introduction

Following great subduction earthquakes, the postseismic surface deformation observed by GNSS and GNSS-A originates from at least three mutually independent primary mechanisms: afterslip, viscoelastic relaxation of the crust and upper mantle, and poroelastic rebound.

Quantitatively separating the contributions of these three deformation mechanisms is one of the core challenges in geodynamics. It is widely accepted that viscoelastic relaxation and afterslip are the two dominant processes for the 2011 Mw 9.0 Tohoku-Oki earthquake, each prevailing across distinct spatiotemporal scales[1-4]. Hu et al.[5] concluded that poroelastic rebound only provides a second-order contribution to postseismic surface displacements. Panuntun et al.[6] further noted that this process largely terminates within approximately 140 days, contributing far less to long-term postseismic deformation than the other two mechanisms. Therefore, poroelastic rebound has relatively limited and short-lived effects on postseismic deformation.

Traditionally, two categories of inversion approaches have been used to interpret postseismic deformation. The first one relies on purely elastic dislocation models, such as the postseismic deformation analysis of the 2011 Tohoku earthquake by Ozawa et al.[7] and Perfettini and Avouac[8]. Such models commonly attribute all observed displacements entirely to fault afterslip and neglect the contribution of mantle viscoelastic relaxation. Subsequent forward modeling by Sun et al.[9] demonstrated that ignoring viscoelastic relaxation systematically overestimates or underestimates afterslip in the downdip and updip directions, indicating that inversions based solely on elastic models contain substantial biases. The second one is the classic two--step inversion method. This one assumes that afterslip and viscoelastic relaxation are

independent processes whose surface deformation signals can be linearly superimposed. The workflow first constrains rheological parameters of deep media using far--field geodetic observations to predict the viscoelastic displacements, and then inverts for the spatial distribution of fault afterslip using the residual signals between the total observed and the predicted displacements. This strategy has been widely applied to postseismic studies of the subduction earthquakes[1-4]. Hu et al.[10] took a trial-and-error calibration scheme to mode the two-year postseismic deformation of the 2011 Mw 9.0 Tohoku-Oki earthquake through a finite element model with the viscoelastic relaxation in the upper mantle and afterslip in a shear zone attached to the megathrust. In their approach, the viscosity of the uniform shear zone to model the afterslip was constrained through repeating earthquakes, and viscosities of the upper mantle were constrained by the GNSS observations. Because of the constant viscosity in the uniform fault shear zone, this approach ignored higher-order heterogeneities in the afterslip distribution. Fukuda and Johnson[11] proposed a Bayesian joint inversion framework treating afterslip and viscoelastic relaxation as a coupled system driven by coseismic stress changes. This framework adopts rate-strengthening friction and the Burgers viscoelastic constitutive relation, enabling simultaneous estimation of contributions from both deformation mechanisms and uncertainty quantification. This method can reproduce the surface deformation of the 2011 Mw 9.0 Tohoku-Oki earthquake, with the advantage of physical self-consistency. However, it still suffers from high computational cost, nonuniqueness in deep parameter inversion, and biases introduced by simplified model geometry, representing important progress in physically constrained postseismic inversion.

Loveless and Meade[12] recently avoided mantle rheology altogether by representing deep viscoelastic effects as equivalent displacement boundary conditions at the base of the elastic layer, and applied this approach to the 1999 Chi-Chi earthquake to simultaneously estimate afterslip on the fault and slip on the basal dislocations that mimic three-dimensional viscous stress dissipation.

Despite these advances, a fundamental methodological challenge remains. Nearly all existing inversions for postseismic slip adopt full Earth models that include the hanging wall, footwall, and viscoelastic mantle. The viscosity used in these models can vary over orders of magnitude, introducing strong nonuniqueness into the inversions.

Based on the earthquake stress model proposed by Xie and Cai[13], we develop a fundamentally different approach from the foregoing methods. For typical cases of surface-rupturing subduction earthquakes where geodetic observations are located only on the hanging wall, there is no need to explicitly model the footwall and mantle or to provide a priori assumptions about poorly constrained rheology of the footwall and mantle. Thus, a hanging-wall-only model is sufficient to investigate postseismic deformation induced by subduction megathrust earthquakes. We apply this model to the 2011 Mw 9.0 Tohoku-Oki earthquake, invert for the tractions on the model boundary surfaces, and separate the surface displacement field generated by afterslip and the one induced by upper mantle viscoelastic relaxation from the total observed surface displacement field.

Results

Using the hanging-wall-only model (Figure 1, Table S1) and the two-year postseismic GNSS[10] and GNSS-A[14] displacement time series (Table S2; representative observed time series are shown in Figure S1) after the 2011 Mw 9.0 Tohoku-Oki earthquake, and applying equal weighting[3] to the observation data within each station for both onshore and seafloor sites, we employ the commercial FEM software COMSOL (http://www.comsol.com) to calculate the synthetic Green's functions and the MATLAB routine lsqlin to invert for the model tractions driving afterslip and viscoelastic relaxation caused by the earthquake. After obtaining the optimal smoothing factor from the L-curve (Figure S2) using the observation data and the above inversion method, we obtained the inverted traction sources (Figure 2, Table S3).

We interpret negative shear and normal tractions on the fault as afterslip sources (strain-energy release), and positive shear and normal tractions as locked sources (strain-energy increase) driven by viscoelastic relaxation in the upper mantle of the subducting slab, and basal shear and normal tractions as mantle-wedge sources arising from viscoelastic relaxation within the upper mantle of the overriding plate. We separate these three traction sources to quantify their individual contributions to surface deformation. Note that in Figure 2, positive shear traction on the fault and on the model basal boundaries is defined along the dip-slip direction and points in the negative direction of the model x-axis**,** respectively, whereas positive normal traction denotes compression on both boundaries.

From Figure 2, we find that spatial heterogeneity exists on both the fault and basal boundaries. During the first postseismic year, the peak decrease and increase in shear traction reach 0.23 MPa for the afterslip source and 0.43 MPa for the locked source on the fault, respectively, whereas normal traction variations (~ 0.045–0.055 MPa) are roughly one order of magnitude smaller. Large reductions near the fault in basal shear traction region span a spatial extent comparable to the coseismic rupture, with a peak magnitude of 0.56 MPa. Outside the reduction zone, the maximum increase in shear traction is 2.0 MPa. Basal normal traction variations are comparable in amplitude to basal shear traction and one order of magnitude larger than fault normal traction variations.

In the second postseismic year, tractions on both the fault and the basal boundary decay markedly. Their spatial patterns remain similar to those of the first year, but peak values are substantially lower. Compared with the first year after the earthquake, the maximum shear traction in the second year decreased by 80% in the afterslip source regions and increased by 69% in the locked source regions. This result indicates that the tractions inducing afterslip are concentrated within the first year following the earthquake and that postseismic deformation mainly occurs within the two years after the earthquake[15]. Notably, the zone of prominent shear traction reduction coincides with the regions of

repeating earthquakes[10,16]. The region with high shear traction and normal tractions falls within the seismogenic zone and rupture area obtained from stress inversion[13,17], indicating intense compression and locking within the rupture zone. Such stress increase on the fault is attributed to the tractions exerted by the subducting slab, which is driven by viscoelastic relaxation in the subducting upper mantle.

Since the model is linearly elastic, the total surface displacement field obeys superposition. Accordingly, the independent surface displacement fields contributed by each of the traction sources can be separated as follows (Figure 3, Table S4).

Afterslip source displacement field (Figure 3a–d): The source drove upward thrust displacements of up to 0.72 m within the peak traction drop patches, and produced normal tensile displacements of up to 0.89 m at the hypocenter and compressive displacements of up to 0.62 m near the trench, north of the hypocenter. It induced horizontal seaward surface displacements of up to 0.57 m in the projection area of the peak traction drop patches. The maximum subsidence (0.86 m) occurred close to the epicenter, while the maximum uplift (0.66 m) occurred near the trench, north of the epicenter.

Locked source displacement field (Figure 3e–h): The source drove landward tangential displacements of up to 1.77 m close to the hypocenter, it induced a maximum landward horizontal surface displacement of 1.42 m near the epicenter. The source drove the normal compressive displacements of up to 1.05 m downdip and to the southwest of the hypocenter and normal tensile displacements of up to 1.01 m close to the trench, east of the hypocenter. The former induced a surface uplift zone with a peak of 1.0 m near the coast west of the epicenter and the latter a surface subsidence zone with a peak of 1.29 m at the trenchward edge of the rupture zone.

Mantle wedge source displacement field (Figure 3i–l): The source drove eastward horizontal displacements of up to 1.15 m in the peak traction drop patches on the model base. It drove normal tensile and compressive displacements, each with a maximum of

0.35 m, at the model base close to the fault. It induced horizontal eastward surface displacements of up to 1.07 m near the epicenter. The maximum subsidence (0.36 m) occurred southwest of the epicenter, while the maximum uplift (0.56 m) occurred near the trench, north of the epicenter.

Figures 3m–p show that the displacement fields between the afterslip source and the mantle wedge source are coupled. The mantle wedge source induced a maximum thrust displacement of 1.07 m and a maximum normal tensile displacement of 0.48 m near the hypocenter, and a maximum normal compressive displacement of 0.44 m north of the hypocenter. This result implies that the displacements on the fault reflect contributions from both the afterslip and mantle wedge sources, with the mantle wedge source contributing more than the afterslip source. The afterslip source induced a maximum basal landward horizontal displacement of 0.63 m close to the fault in the central part of the model bottom, and the maximum vertical tensile and compressive displacements of 0.45 m and 0.39 m close to the fault in the southern and northern parts, respectively.

Overall, the greatest contribution (Figure 3g) to the surface displacements came from the locked source, followed (Figure 3k) by the mantle wedge source, and the smallest (Figure 3c) was from the afterslip source. Surface subsidence was greater than surface uplift for all three sources. The maximum subsidence (Figure 3h) close to the trench near the epicenter originated from the locked source, and the minimum (Figure 3i) from the mantle wedge source. The fault tangential displacements (Figure 3h) from the locked source were greater than those from the mantle wedge source and the afterslip source.

Full details and peak values of the displacement field for each source are provided in Figures S3–S6.

Figure 4 and Table S5 show that the equal-weight inversion results fit well for all three datasets—onshore, seafloor, and the combined onshore–seafloor (All) set. However, the seafloor residuals have noticeably larger biases: in particular, the EW component

shows a local systematic bias, and the NS component has relatively large random errors. For the onshore and combined datasets, the residual means are at the sub-millimeter level and the variances are much smaller than the observed variances, indicating stable fits. Overall, the model explains most of the displacement signal. The seafloor fit is slightly less reliable than the onshore horizontal components, but this mainly reflects observation noise and signal strength rather than model failure. Figures 4e–h show that the surface horizontal (Figure 4e) and vertical (Figure 4h) displacement fields each equal the sum of the respective fields generated by the fault and the base. The calculated surface horizontal and vertical displacements at the observation points agree with the onshore GNSS and seafloor GNSS-A observations in Figures 4a and b. These results demonstrate that the surface displacement field produced by the model tractions obeys the principle of elastic superposition.

Discussion and Conclusions

Residual and variance analyses between the model predictions and observations confirm the reliability of the inversion results. The onshore and seafloor horizontal components have small residual means, variances consistent with the observations, and Pearson correlation coefficients above 0.99, indicating stable and reliable modeling of horizontal deformation. The seafloor vertical component is also highly credible, with a coefficient of 0.998. The onshore vertical component has a lower correlation coefficient (0.935) but still indicates a strong correlation; this lower value mainly reflects the intrinsically low signal-to-noise ratio of GNSS vertical measurements and does not affect the overall conclusions. In addition, the relatively large residual means for the seafloor data suggest a possible local systematic bias in the seafloor simulation, making its credibility slightly lower than that of the onshore horizontal components; these issues may arise from insufficient local model resolution, uneven seafloor data coverage, and the low signal-to-noise ratio of vertical observations.

The checkerboard resolution test (Figure S7) shows that the model bottom and fault sub-sources are well recovered, with only a few sub-sources in the northeast corner of the fault and along the northwestern edge of the bottom boundary exhibiting recovered

tractions below 0.4 MPa. This suggests relatively insufficient local resolution in these edge or poorly covered areas. The maximum residual between the predicted displacements and the displacements produced by a unit stress with 1% standard deviation does not exceed 1% (Figure S8).

The statistical results for the three traction components of the checkerboard input model (mean = 0, variance = 1; Table S6) show output means of −0.0375, −0.0177, and −0.00065, all close to zero, indicating no significant long-wavelength spurious traction anomalies in the inversion results. The output variances are 0.754, 0.783, and 0.929, all smaller than the input variance of 1; the regression slopes k are 0.739, 0.771, and 0.885, corresponding to amplitude recoveries of approximately 74%, 77%, and 89%, with component z recovering best and component x showing the strongest compression. The correlation coefficients between the output and input are 0.852, 0.871, and 0.919, indicating that the alternating positive–negative pattern is well recovered in all three components without overall misalignment or sign reversal. The residual variances are 0.275, 0.242, and 0.158, all smaller than the input variance of 1, indicating that the recovered tractions are generally close to the input tractions; however, as a global statistic, residual variance cannot guarantee good recovery at every node, and local smoothing or small-scale misalignment may remain. Taken together, Figures S7 and S8 and Table S3 indicate that the checkerboard resolution test results are generally good and that the inversion results for the 2011 Mw 9.0 Tohoku-Oki earthquake are reliable.

A major limitation arises from defining the base of the elastic layer at the model lower boundary of 47 km, the transition depth of the fault dip angle from 10° to 30°, which does not represent the actual top of the upper mantle. Although this depth is consistent with the elastic-layer depth of ~50 km[2, 18, 19] used in previous studies, the effect of this depth choice on the inverted tractions warrants further study.

We assign equal weighting to horizontal and vertical displacements across all observation stations. This effectively lowers the weight for postseismic seafloor displacement data simply because there are vastly fewer seafloor observation sites compared with onshore ones. Although quantitative assessment of the uncertainty for

seafloor observations remains challenging, seafloor measurements are almost certainly less accurate than onshore observations, and we adopt this weighting scheme to reflect this consideration[3].

The inversion results reveal strongly heterogeneous and rapidly decaying postseismic traction adjustment, with the largest traction changes in the first year and a marked decline in the second. It should be noted that the inverted traction includes tectonic loading. However, the shear component of the tectonic loading on the fault is nearly an order of magnitude smaller[17] than that of the inverted traction. Therefore, the inverted traction is mainly influenced by postseismic viscoelastic relaxation and afterslip. The displacement field produced by mantle viscoelastic relaxation is greater than that of afterslip in the two years after the earthquake. The zones of reduced fault shear traction coincide with repeating-earthquake clusters and represent afterslip unloading, whereas the zones of simultaneous increases in shear and normal traction fall in the seismogenic zone and coseismic rupture area, indicating postseismic stress accumulation and locking. This traction increase can be interpreted as loading of the locked zone caused by viscoelastic stress relaxation within the upper mantle of the subducting plate. This outcome may provides direct quantitative constraints for assessing the stress loading rate of future strong earthquakes in the region and determining the earthquake recurrence interval.

Overall, the inverted tractions represent an optimal equivalent mechanical description instead of a unique solution. Even so, our results demonstrate that this approach can still isolate the contributions of different traction sources to the deformation field. The method is physically self-consistent and free of prior rheological assumptions, and it can be extended to other large subduction thrust earthquakes.

Method

Based on the earthquake stress model[13], we construct an overriding-plate-only finite element (FEM) model (Figure 1). The model domain terminates at the base of the overriding lithosphere; the mantle wedge is excluded from the computational domain. In this study, postseismic deformation is treated as a quasi-static viscoelastic infinitesimal deformation process, at any given time, this problem reduces to a static boundary-value problem. Thus, the model boundary conditions are time-independent, which are specified as follows: the surface is free; the western lateral boundary is fixed and located far enough from the fault; and the surface-breaking fault boundary and the basal truncation boundary of the model together serve as the two traction boundaries on which the tractions are inverted. Hereafter in the inversion, regions where the tractions on the fault decrease and increase are defined as the afterslip source and locking source, respectively; the equivalent viscoelastic tractions on the basal truncation boundary, referred to as the mantle-wedge traction boundary, are termed the mantle-wedge source. Given that postseismic deformation is driven by stress changes, the term "traction" on the boundaries of the model refers to stress change in this study.

We compute numerical Green's functions using the finite element method. First, we discretize the megathrust fault and the basal model boundary into mesh cells. Second, we precompute individual elastic displacement Green's functions for traction components on each cell. Each Green's function describes the surface displacement response at observation stations, induced by a unit traction component applied to one boundary cell. Third, we linearly superimpose all Green's functions to assemble the numerical Green's function matrix $\mathbf{G}$ for inversion and form the governing equation for the traction source:

$$\mathbf{GT} = \mathbf{d}$$

where $\mathbf{d}$ denotes observed postseismic displacements. We solve for the optimal traction field by minimizing the misfit between modeled and observed displacements.

A smoothness regularization constraint, $\mathbf{LT} = \mathbf{0}$, is further introduced to suppress spatial oscillations of the solution and mitigate the ill-posedness of the inversion, where $\mathbf{L}$ represents the Laplacian operator matrix[20]. Since the fault cannot physically undergo normal opening or penetration, we impose a zero normal displacement constraint on the fault interface, $\mathbf{G}_n\mathbf{T} = \mathbf{0}$, where $\mathbf{G}_n$ is the submatrix of the fault Green's function matrix, corresponding to normal displacement components. Thus, we can set up an objective function for the least-squares problem with smoothness regularization and equality constraints

$$\varphi = \|\mathbf{W}_d(\mathbf{GT} - \boldsymbol{d})\|^2 + \lambda\|\mathbf{LT}\|^2 + 2\boldsymbol{\beta}^T(\mathbf{G}_n\mathbf{T} - \mathbf{0})$$

where $\mathbf{W}_d$ is the data weighting matrix (usually diagonal, with elements being the reciprocals of data errors), λ is the smoothing factor (regularization parameter), $\boldsymbol{\beta}$, a Lagrange multiplier vector[21]. Note that the factor 2 in front of the constraint term is for convenience in subsequent differentiation. Then, we take derivatives with respect to $\mathbf{T}$ and $\boldsymbol{\beta}$, and set them to zero:

$$\begin{aligned}\frac{\partial\varphi}{\partial\mathbf{T}} &= 2\mathbf{G}^T\mathbf{W}_d^T\mathbf{W}_d(\mathbf{GT}-\mathbf{d}) + 2\lambda\mathbf{L}^T\mathbf{LT} + 2\mathbf{G}_n^T\boldsymbol{\beta} = \mathbf{0}\\ \frac{\partial\varphi}{\partial\boldsymbol{\beta}} &= 2\mathbf{G}_n\mathbf{T} = \mathbf{0}\end{aligned}$$

Arranging gives the following linear system

$$\begin{bmatrix}\mathbf{G}^T\mathbf{W}_d^T\mathbf{W}_d\mathbf{G} + \lambda\mathbf{L}^T\mathbf{L} & \mathbf{G}_n^T\\ \mathbf{G}_n & \mathbf{0}\end{bmatrix}\begin{bmatrix}\mathbf{T}\\ \boldsymbol{\beta}\end{bmatrix} = \begin{bmatrix}\mathbf{G}^T\mathbf{W}_d^T\mathbf{W}_d\mathbf{d}\\ \mathbf{0}\end{bmatrix}$$

Solving this system yields the traction $\mathbf{T}$ and $\boldsymbol{\beta}$ for a given λ. Determining the optimal λ is usually based on balancing the data misfit term and the model smoothing term. A common approach is the L-curve method, which plots the data misfit residual $\mathbf{W}_d(\mathbf{GT}-\mathbf{d})$ versus the model smoothing term $\mathbf{LT}$, and selects the λ corresponding to

the point of maximum curvature. It should be noted that equality constraints affect the curve shape, but the corner still represents the best trade-off.

Data availability

The GNSS daily time series were obtained from the Nevada Geodetic Laboratory (https://geodesy.unr.edu/). The GNSS-A data were obtained from JHOD (https://www1.kaiho.mlit.go.jp/chikaku/kaitei/sgs/gnss-a_timeseries_e.html). Processed GNSS data are presented in the supplementary material.

Author contributions

X.Z. performed the finite element forward modeling, inversion, and visualization. Y.H. contributed to data analysis. Y.C. proposed the inversion method and model construction, and supervised the research. The manuscript was drafted by Y.C. and edited by X.Z., Y.H. All authors contributed to theoretical interpretation.

Acknowledgements

This study was supported by Natural Science Foundation of China (grant 42274125). YH was supported by Natural Science Foundation of China (grant 42374111) and 2024 Jianghuai Talent Development Program Outstanding Project. We thank Shoichi Yoshioka for his providing the original GNSS data. Some figures were plotted by using GMT[22].

Competing interests

The authors declare no competing interests.

References

1. Sun, T. & Wang, K. Viscoelastic relaxation following subduction earthquakes and its

effects on afterslip determination. J. Geophys. Res. Solid Earth 120, 1329–1344 (2015). https://doi.org/10.1002/2014JB011707

2. Yamagiwa, S., Miyazaki, S., Hirahara, K. & Fukahata, Y. Afterslip and viscoelastic relaxation following the 2011 Tohoku-oki earthquake (Mw9.0) inferred from inland GPS and seafloor GPS/Acoustic data. Geophys. Res. Lett. 42, 66–73 (2015). https://doi.org/10.1002/2014GL061735
3. Freed, A. M., Hashima, A., Becker, T. W., Okaya, D. A., Sato, H. & Hatanaka, Y. Resolving depth-dependent subduction zone viscosity and afterslip from postseismic displacements following the 2011 Tohoku-Oki, Japan earthquake. Earth Planet. Sci. Lett. 459, 279–290 (2017). https://doi.org/10.1016/j.epsl.2016.11.040
4. Barbot, S. Asthenosphere flow modulated by megathrust earthquake cycles. Geophys. Res. Lett. 45, 6018–6031 (2018). https://doi.org/10.1029/2018GL078197
5. Hu, Y., Bürgmann, R., Freymueller, J. T., Banerjee, P. & Wang, K. Contributions of poroelastic rebound and a weak volcanic arc to the postseismic deformation of the 2011 Tohoku earthquake. Earth Planets Space 66, 106 (2014). https://doi.org/10.1186/1880-5981-66-106
6. Panuntun, H., Miyazaki, S., Fukuda, Y., & Orihara, Y. Probing the Poisson‘s ratio of poroelastic rebound following the 2011 Mw 9.0 Tohoku earthquake. Geophys. J. Int. 215 (3), 2206–2221 (2018). https://doi.org/10.1093/gji/ggy403
7. Ozawa, S., Nishimura, T., Suito, H., Kobayashi, T., Tobita, M. & Imakiire, T. Coseismic and postseismic slip of the 2011 magnitude-9 Tohoku-Oki earthquake. Nature 475, 373–376 (2011). https://doi.org/10.1038/nature10227
8. Perfettini, H. & Avouac, J. P. The seismic cycle in the area of the 2011 Mw9.0 Tohoku-Oki earthquake. J. Geophys. Res. Solid Earth 119, 4469–4515 (2014). https://doi.org/10.1002/2013JB010697
9. Sun, T. et al. Prevalence of viscoelastic relaxation after the 2011 Tohoku-oki earthquake. Nature 514, 84–87 (2014). https://doi.org/10.1038/nature13778
10. Hu, Y., Bürgmann, R., Uchida, N., Banerjee, P. & Freymueller, J. T. Stress-driven relaxation of heterogeneous upper mantle and time-dependent afterslip following the

2011 Tohoku earthquake. J. Geophys. Res. Solid Earth 121, 385–411 (2016). https://doi.org/10.1002/2015JB012508

11. Fukuda, J. & Johnson, K. M. Bayesian inversion for a stress-driven model of afterslip and viscoelastic relaxation: Method and application to postseismic deformation following the 2011 MW 9.0 Tohoku-Oki earthquake. J. Geophys. Res. Solid Earth 126, e2020JB021620 (2021). https://doi.org/10.1029/2020JB021620
12. Loveless, J. P. & Meade, B. J. Kinematic representations of viscoelastic postseismic deformation. Earth Space Sci. 12, e2025EA004460 (2025). https://doi.org/10.1029/2025EA004460
13. Xie, Z. & Cai, Y. Inverse Method for Static Stress Drop and Application to the 2011 Mw9.0 Tohoku-Oki Earthquake. J. Geophys. Res. Solid Earth 123, 2871–2884 (2018). https://doi.org/10.1002/2017JB014871
14. Yokota, Y., Ishikawa, T. & Watanabe, S. Seafloor crustal deformation data along the subduction zones around Japan obtained by GNSS-A observations. Sci. Data 5, 180182 (2018). https://doi.org/10.1038/sdata.2018.182
15. Watanabe, S., Ishikawa, T., Nakamura, Y. & Yokota, Y., Co- and postseismic slip behaviors extracted from decadal seafloor geodesy after the 2011 Tohoku-oki earthquake. Earth Planets Space 73, 162 (2021). https://doi.org/10.1186/s40623-021-01487-0
16. Uchida, N., Shimamura, K., Matsuzawa, T. & Okada, T. Postseismic response of repeating earthquakes around the 2011 Tohoku-oki earthquake: Moment increases due to the fast loading rate. J. Geophys. Res. Solid Earth 120, 259–274 (2015). https://doi.org/10.1002/2013JB010933
17. Xie, Z., Cai, Y., Wang, C.-Y., Yoshioka, S. & Tanaka, M. Fault stress inversion reveals seismogenic asperity of the 2011 Mw 9.0 Tohoku-Oki earthquake. Sci. Rep. 9, 11987 (2019). https://doi.org/10.1038/s41598-019-47992-x
18. Diao, F., Xiong, X., Wang, R., Zheng, Y., Walter, T. R., Weng, H. & Li, J. Overlapping post-seismic deformation processes: Afterslip and viscoelastic relaxation following the 2011 Mw 9.0 Tohoku Japan earthquake. Geophys. J. Int. 196, 218–229 (2014).

https://doi.org/10.1093/gji/ggt376

19. Shirzaei, M., Bürgmann, R., Uchida, N., Hu, Y., Pollitz, F. & Matsuzawa, T. Seismic versus aseismic slip: probing mechanical properties of the northeast Japan subduction zone. Earth Planet. Sci. Lett. 406, 7–13 (2014). https://doi.org/10.1016/j.epsl.2014.08.035
20. Masterlark, T. Finite element model predictions of static deformation from dislocation sources in a subduction zone: Sensitivities to homogeneous, isotropic, Poisson-solid, and half-space assumptions. J. Geophys. Res. Solid Earth 108(B11), 2540 (2003). https://doi.org/10.1029/2002JB002296
21. Cai, Y., He, T. & Wang, R. Numerical simulation of dynamic process of the Tangshan earthquake by a new method—LDDA. Pure Appl. Geophys. 157, 2083–2104 (2000). https://doi.org/10.1007/PL00001076
22. Wessel, P., & W. H. F. Smith, New, improved version of the Generic Mapping Tools released, Eos Trans. AGU, 79, 579 (1998). https://doi.org/10.1029/98EO00426

Figure Caption

Figure 1. Traction source model for inverting postseismic deformation (modified from Xie and Cai[13]). a, Study region of postseismic deformation. Magenta dots denote GNSS stations. The brown rectangle marks the repeating earthquake region, where the numbers indicate the numbers of repeating earthquakes. The blue star denotes the epicenter of the 2011 Mw 9.0 Tohoku-Oki earthquake on March 11, 2011, and yellow dots denote the location of seafloor GNSS-A sites. Data from the six stations within white circles in **a** are shown in Figure S1. The letters a, b, c, d, e, and f denote stations J910, J201, J195, KAMN, MYGW and FUKU, respectively. **b**, Finite element model, with a fault dip angle of 11°, the top and bottom boundaries extend 850 and 800 km in the x direction, respectively, and 1200 km in the y direction. The model bottom is at 47 km, representing the average depth of the uppermost upper mantle. **c**, Traction subsources on the fault and at the bottom are marked by light purple and light blue. Both the fault subsources and bottom subsources have

441 dimensions of about 63 km × 50 km. The blue star indicates the hypocenter location.

442

443

444 **Figure 2. Inverted traction sources for the two years following the Tohoku-Oki earthquake**.

445 **a**–**d**, show changes in fault shear stress, fault normal stress, basal shear stress, and basal normal

446 stress from 12 March 2011 to 12 March 2012. **e**–**h**, show the same quantities from 12 March 2012

447 to 12 March 2013.

448

449 **Figure 3. Displacement fields calculated from three types of the inverted traction sources**. **a**–

450 **d**, show displacement fields of the afterslip source. **e**–**h**, The locked source. **i**–**l**, The mantle wedge

451 source. For the first and second rows, each column sequentially presents fault tangential

452 displacement, fault-normal displacement, surface tangential displacement, and surface vertical

453 displacement. For the third row, each column sequentially presents basal tangential displacement,

454 basal vertical displacement, surface tangential displacement, and surface vertical displacement. **m**

455 and **n** show displacement fields on the fault, induced by the mantle wedge source, and **o** and **p** show

456 displacement fields on the basal surface induced by the afterslip and locked sources on the fault.

457

458 **Figure 4. Observed and predicted surface displacements for the first postseismic year. a** and **b**,

459 Displacement fitting. **c** and **d**, Residuals of observation and predicted displacements. **e** and **h**,

460 Surface horizontal and vertical displacement fields calculated from all inverted traction sources; **f**

461 and **i**, from the fault traction sources only; and **g** and **j**, from the basal traction sources only. **e** is the

462 sum of **f** and **g**. **h** is the sum of **i** and **j**.

463

464

465

466

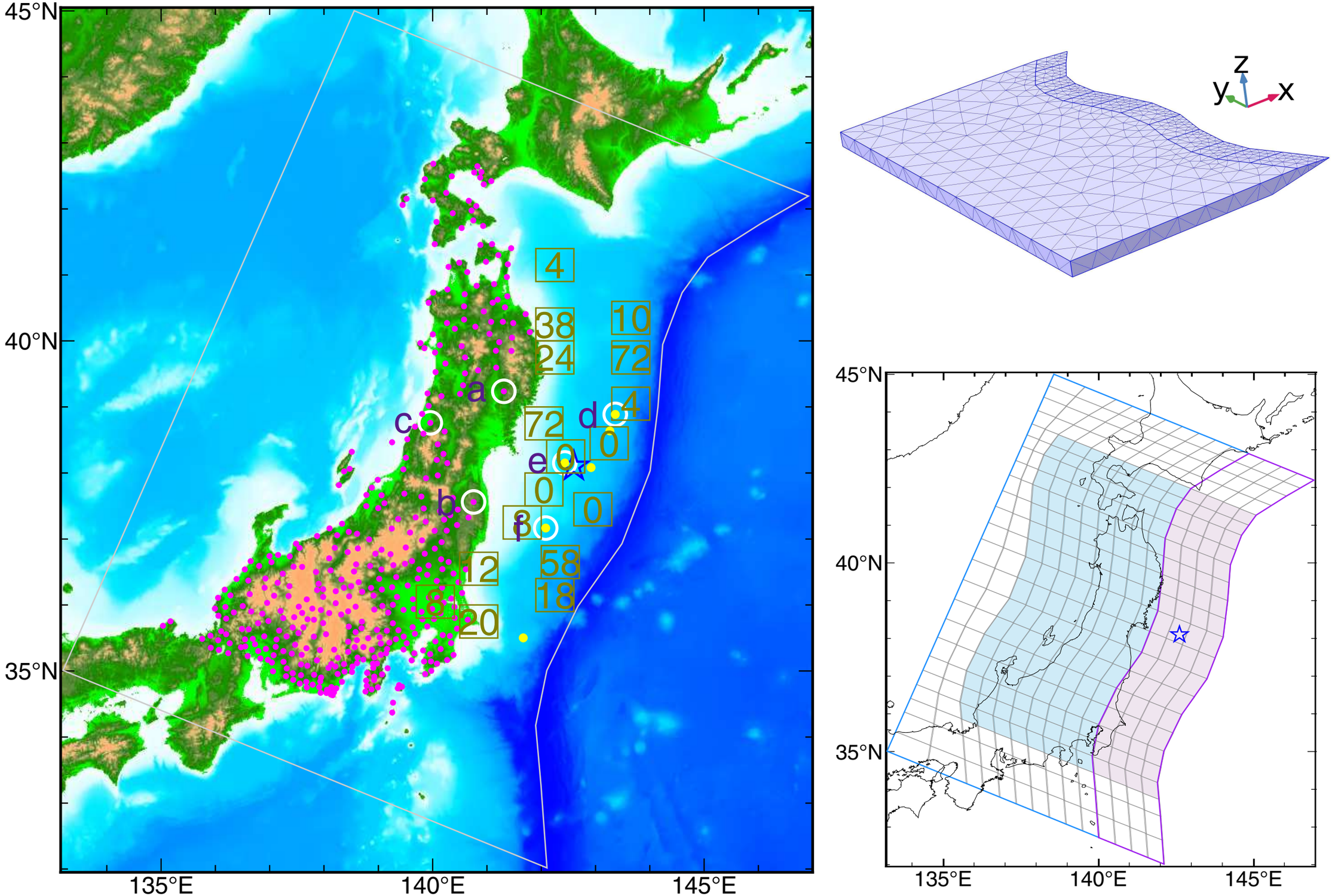
45°N
40°N
35°N
135°E
140°E
145°E
4
38
24
10
72
a
c
72
d
4
0
e
0
0
b
0
f
58
12
18
8
20
z
y
x
45°N
40°N
35°N
135°E
140°E
145°E

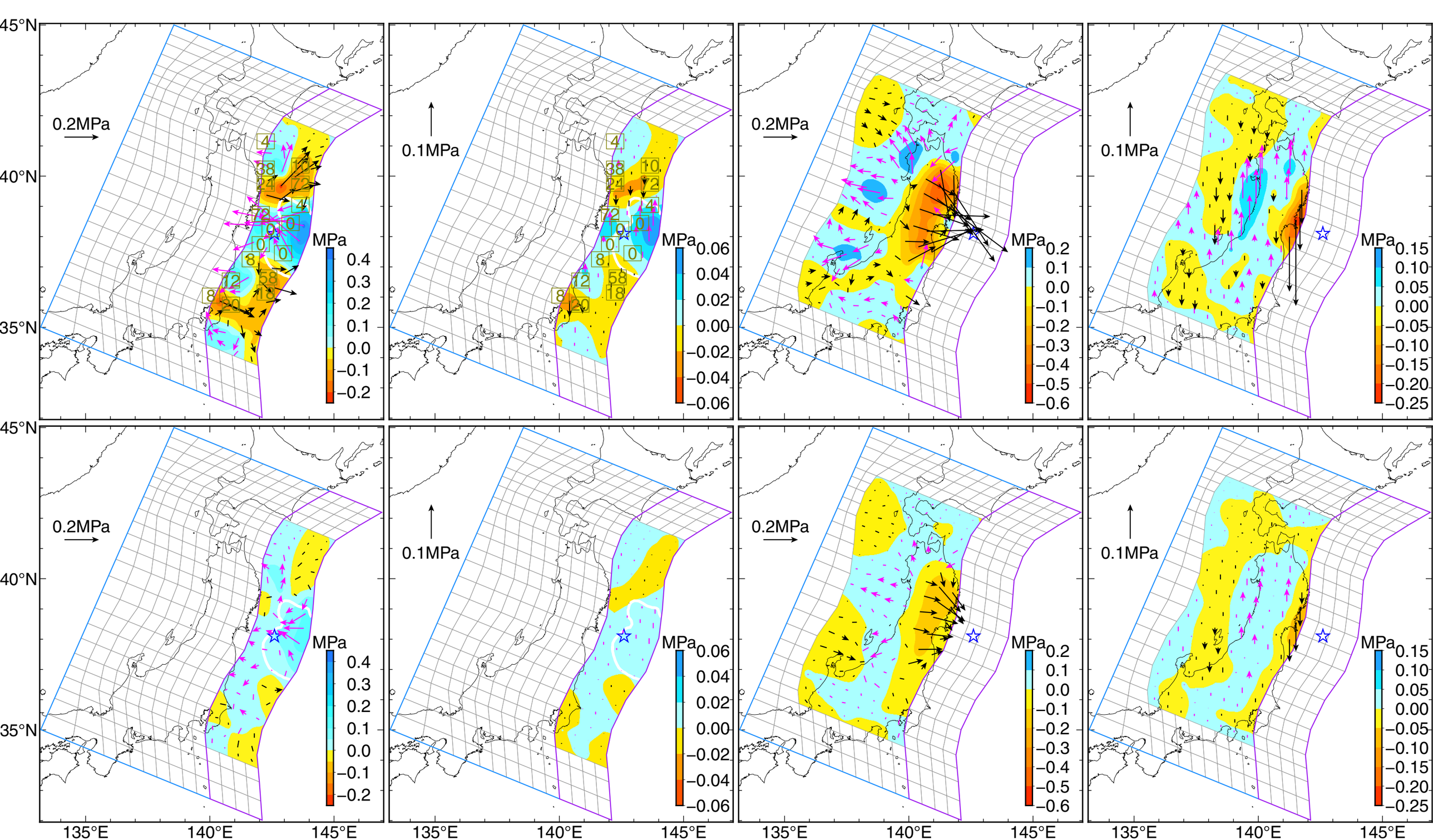
45°N
40°N
35°N
135°E
140°E
145°E
0.2MPa
0.1MPa
MPa
0.4
0.3
0.2
0.1
0.0
−0.1
−0.2
0.06
0.04
0.02
0.00
−0.02
−0.04
−0.06
0.15
0.10
0.05
−0.05
−0.10
−0.15
−0.20
−0.25
−0.3
−0.4
−0.5
−0.6

45°N
40°N
35°N
135°E
140°E
145°E
1m
0.5m
m

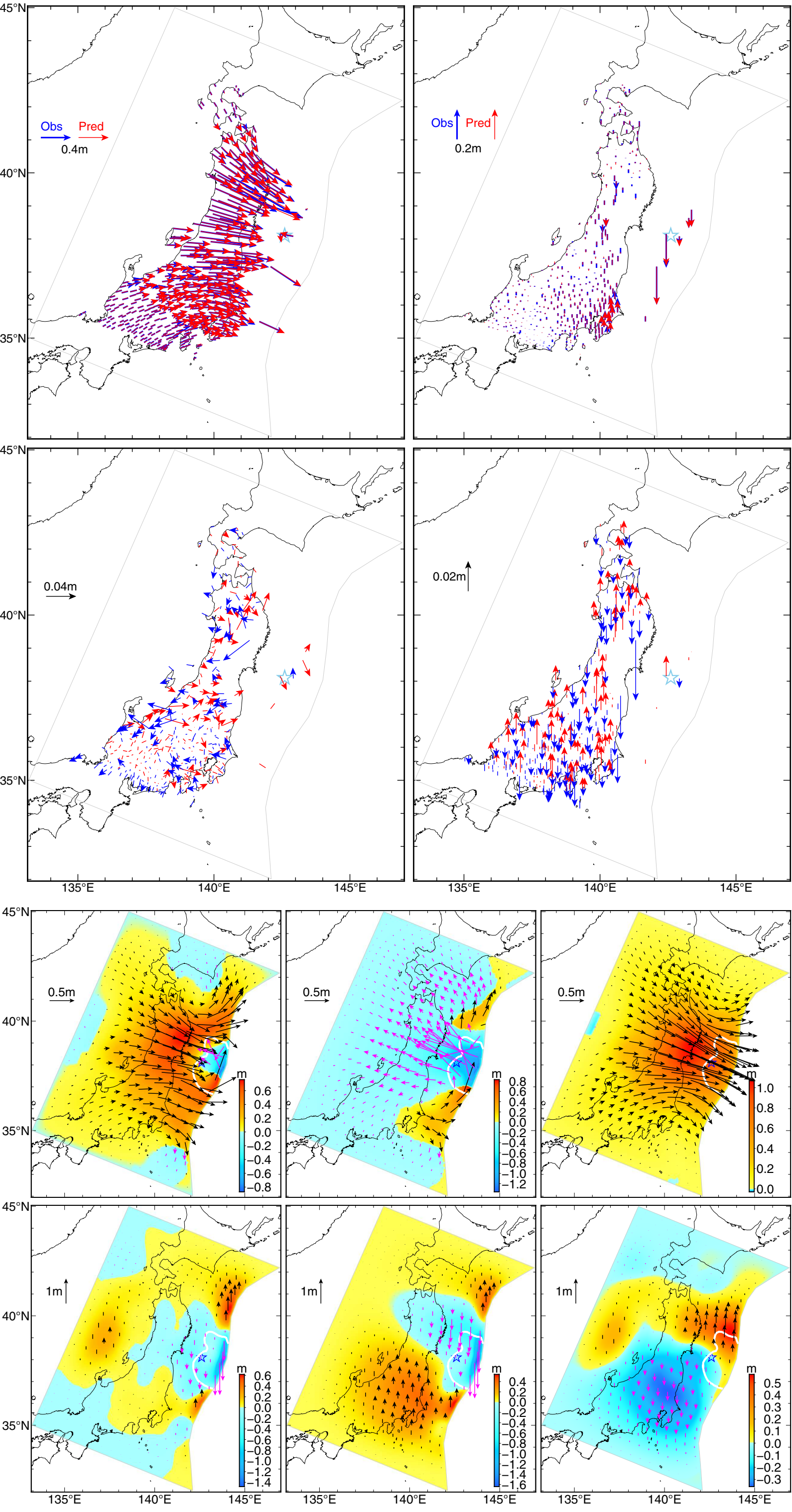
Obs
Pred
0.4m
Obs
Pred
0.2m
0.04m
0.02m
0.5m
0.5m
0.5m
1m
1m
1m
m
45°N
40°N
35°N
135°E
140°E
145°E

Supplementary Files

This is a list of supplementary files associated with this preprint. Click to download.

- SUPPLEMENTINFORMATION20261119.docx